Journal of Translational Medicine

RESEARCH

Open Access

ITGB5-mediated biomechanical regulation in pancreatic ductal adenocarcinoma stroma impacts tumor progression and prognosis

Aoran Yang[1,2†], Chengli Gu[1,2†], Yining Liu[1,2†], Baihe Luo[1,2], Yu Zeng[1,2], Minghui Zhou[1,2], Chunli Li[1,2], Chen Pan[1,2], Linxuan Wu[1,2,3], Zhiwen Hu[1,2], Xin Zhang[4*], Feng Gao[5*] and Yu Shi[1,2*]

Abstract

Background Pancreatic ductal adenocarcinoma (PDAC) is characterized by stromal remodelling andstiffening, a process involving extracellular matrix (ECM) depositionand cross-linking, which forms a dense physical barrier that limits the penetration of chemotherapeutic agents and restricts immune cell-mediated cytotoxicity. In addition, the tumor stroma modulates nutrients availability and fosters cancer cell invasion and metastasis. Therefore, therapeutic strategies aimed at modulating the tumor stroma hold promise for overcoming some of the major challenges in pancreatic cancer treatment. However, most clinical trials of stromal-targeted therapies have not demonstrated meaningful improvements in overall survival, underscoring an urgent need to identify novel stromal targets and approaches that modulate the tumor microenviroment in ways that enhance therapeutic response and improve patient outcomes.

Methods Transcriptomic datasets of PDAC sampleswere obtained from The Cancer Genome Atlas (TCGA). By integrating immune infiltration algorithms with weighted gene co-expression network analysis (WGCNA), this study aims to identify hub genes associated with cancer-associated fibroblasts (CAFs) infiltration in PDAC, explore the prognostic relevance of CAF infiltration, and construct a gene-expression-based prognostic mode. Furthermore, we will employ a multi-modal approach incorporating magnetic resonance elastography, atomic force microscopy, single-cell RNA sequencing (scRNA-seq), histological assays, cell-based functional experiments, and animal models to identify candidate core genes involved in CAF infiltration and stromal stiffening in pancreatic cancer, and to assess the potential therapeutic relevance of targeting these genes.

Results In PDAC, increased stromal stiffness and poor prognosis are both strongly linked to activation of CAFs. WGCNA identified six hub genes—*ANTXR2, ANXA1, BCAT1, PLAU, TGFβ1*, and *ITGB5*—which were used to construct a

†Aoran Yang, Chengli Gu and Yining Liu contributed equally to this research.

*Correspondence:
Xin Zhang
zhangxin_2003@163.com
Feng Gao
gaof@sj-hospital.org
Yu Shi
20072265@cmu.edu.cn

Full list of author information is available at the end of the article

© The Author(s) 2025. **Open Access** This article is licensed under a Creative Commons Attribution-NonCommercial-NoDerivatives 4.0 International License, which permits any non-commercial use, sharing, distribution and reproduction in any medium or format, as long as you give appropriate credit to the original author(s) and the source, provide a link to the Creative Commons licence, and indicate if you modified the licensed material. You do not have permission under this licence to share adapted material derived from this article or parts of it. The images or other third party material in this article are included in the article's Creative Commons licence, unless indicated otherwise in a credit line to the material. If material is not included in the article's Creative Commons licence and your intended use is not permitted by statutory regulation or exceeds the permitted use, you will need to obtain permission directly from the copyright holder. To view a copy of this licence, visit http://creativecommons.org/licenses/by-nc-nd/4.0/.

predictive model for estimating CAF abundance and forecasting PDAC prognosis. Single-cell RNA sequencing analysis showed that *ITGB5* is highly expressed in CAFs. Both in vitro and in vivo experiments demonstrated that targeting *ITGB5* in CAFs reduces tumor stiffness, thereby inhibiting the malignant progression of PDAC. These findings suggest a potential therapeutic benefit, although impact on clinical prognosis remains to be established.

Conclusion The integration of magnetic resonance elastography, atomic force microscopy, and single-cell sequencing allows detailed research characterization of the biomechanical properties of PDAC. *ITGB5* has been identified as an important regulator of the biomechanical features of PDAC. Targeting *ITGB5* in CAFs may reduce the excessive stiffness of PDAC tissue and mitigate gemcitabine-associated stromal fibrosis, suggesting a potential strategy to improve treatment response. The effect on patient prognosis, however, requires confirmation in clinical studies.

Trial registration This study is a prospective single-center clinical trial, which has been registered in the U.S. Clinical Trials Database (https://clinicaltrials.gov/study/NCT06526442) with the trial registration number NCT06526442. The registration date was October 9th, 2020.

Keywords ITGB5, Tumor biomechanics, Single-cell RNA sequencing, Pancreatic ductal adenocarcinoma, Biomechanical biomarkers

Introduction

Pancreatic ductal adenocarcinoma (PDAC) is the most common exocrine malignancy of the pancreas. Because symptoms are often subtle and the pancreas is anatomically concealed, PDAC is usually diagnosed at an advanced stage. The overall 5-year survival rate remains approximately 13% according to recent epidemiological data [1]. The aggressive clinical course of PDAC is partly attributable its complex tumor microenvironment [2], which involves the activation of a large number of cancer-associated fibroblasts (CAFs) that secrete abundant collagen fibers [3]. On one hand, these collagen fibers provide essential nutrients for tumor growth, such as branched-chain amino acids [4], that support tumor growth. On the other hand, the dense stromal barrier impairs drug delivery and efficacy [5], suppresses immune responses [6], and facilitates tumor immune evasion. Additionally, the accumulation of collagen fibers contributes to the "stiff" biomechanical characteristics of PDAC [7], a phenomenon that is also observed, though to varying degrees, in other tumors such as breast cancer [8]. This biomechanical phenotype can be described by four aspects [9]: elevated tissue stiffness, increased solid pressure, heightened interstitial fluid pressure, and altered extracellular matrix architecture in tumor microstructure.

For PDAC, these four factors contribute to intratumoral hypoxia, stabilization and activation of HIF-1α activation of *HIF-1α*, and the enhancement of malignant traits such as invasion, metastasis, and resistance to therapy in PDAC [10]. Additionally, the intense pressure compresses blood vessels, reducing vessel patency and perfusion, which hinders the effective delivery of chemotherapeutic agents to the tumor, leading to poor prognosis. Therefore, the biomechanical characteristics of PDAC are increasingly recognized as potential diagnostic or prognostic indicators, and may also represent novel therapeutic targets [11].

Currently, there are several methods to assess the biomechanical characteristics of PDAC, including endoscopic ultrasound elastography [12], atomic force microscopy [13], Shore durometer measurements [14], and histopathological assessment of extracellular matrix remodeling. However, many of these approaches are invasive or minimally invasive, and both atomic force microscopy and histopathological assessment rely on tissue sampling, which are limited by the pronounced spatial heterogeneity of PDAC, often leading to sampling bias [15]. 3D magnetic resonance elastography (3D-MRE) has been extensively applied in the clinical diagnosis and treatment staging of liver fibrosis [16]. It is non-invasive, clinically feasible and provides macroscopic-scale measurements that reduce the impact of tumor heterogeneity.

Integrin Beta-5 (ITGB5) is a gene encoding the integrin β5 subunit, which forms heterodimeric receptors with specific α subunits and participates in cellular adhesion and signaling. For example, in gastric cancer, *ITGB5* has been reported as a prognostic biomarker and promotes tumor progression via *TGFBR2* [17]. In oral cancer, *ITGB* 5contributes to tumorigenesis and disease progression [18]. Notably, previous studies have demonstrated that *ITGB5* plays a significant role in PDAC. For instance, acetylation-mediated modification of *ITGB*5 enhances perineural invasion in PDAC, leading to poor prognosis [19]. Additionally, *ITGB5* confers radiotherapy resistance by promoting DNA damage repair and activating the *MEK/ERK* signaling pathway [20]. These findings support *ITGB5* as a potential therapeutic target in PDAC. However, the impact of ITGB5 on the biomechanical properties of PDAC and its potential as a stromal-targeting therapeutic strategy remain insufficiently explored. Therefore, this study investigates how *ITGB5* regulates

biomechanical characteristics of PDAC and contributes to malignant progression.

Materials and methods

Patient selection and PDAC sample collection

The inclusion criteria for PDAC patients were consistent with those applied in our previous study [21]. Briefly, Inclusion criteria were as follows: (1) Histologically confirmed PDAC; (2) Main pancreatic duct (MPD) diameter ≥ 3 mm; (3) Age ≥ 18 years and ≤ 80 years; (4) No history of extra pancreatic malignant tumors; (5) No prior neoadjuvant chemotherapy, radiotherapy, or biliary drainage before surgery. Exclusion criteria were as follows: (1) Inability to maintain adequate breath-holding or intolerance to the mechanical driver stimulus required for MRE; (2) Tumor diameter < 10 mm; (3) Contraindications to magnetic resonance imaging (e.g., claustrophobia). Ultimately, 80 PDAC patients with a median age of 60 years (range, 35–79 years) and a median body mass index of 21.66 kg/m_2 (range, 16.60–28.70 kg/m^2), were included in this study. Detailed information is provided in Table S1. Fresh tumor tissues were obtained during surgery and either snap-frozen in liquid nitrogen or stored in preservation solution for subsequent analyses.

Isolation of primary CAFs and conditioned medium collection

For freshly collected PDAC tissues, the tissues were first rinsed 3–5 times with PBS to remove blood, and then minced into approximately 1 mm^3 pieces with sterile scissors. The samples were dissociated using a SeekMate A pro (Beijing, China) and filtered through a 70-μm sterile cell strainer. Subsequently, Anti-LUM IgG primary antibody was added according to the protocol, incubated at 4 °C for 30 min, and unbound antibodies were removed by elution. After cell counting, 20 μl of Anti-mouse IgG-conjugated magnetic beads were added per 110^7 cells and incubated at 4 °C for 15 min to allow the magnetic beads to bind to the antibodies attached to cell surface antigens. MACS separation columns were then used to sort and collect LUM-positive cells. The collected cells were transferred to a 6-well plate and cultured in Dulbecco's modified Eagle medium supplemented with 15% fetal bovine serum and 1% penicillin–streptomycin to grow CAFs.

Approximately 5×10^6 CAFs were seeded in a 10-cm dish until ~ 70–80% confluence. Cells were then washed and incubated in serum-free DMEM for 48 h. Then the conditioned medium (CM) was collected and centrifuged to remove cell pellets. CFPAC-1 and Mia Paca-2 cells were then cultured with the CM (refreshed every 2–3 days) for 2 weeks before being used in experiments.

Cell culture

The human PDAC cell lines (CFPAC-1, Mia Paca-2) were purchased from Procell biotechnology company (Wuhan, China). CFPAC-1 cells were cultured in Iscove's Modified Dulbecco's Medium (IMDM) supplemented with 10% fetal bovine serum and 1% penicillin–streptomycin. Mia Paca-2 cells were maintained in Dulbecco's modified Eagle medium (DMEM) supplemented with 10% fetal bovine serum and 1% penicillin–streptomycin. CAFs were cultured in DMEM supplemented with 15% FBS and 1% penicillin–streptomycin. All cells were maintained in a humidified incubator containing 5% CO_2 at 37 °C.

Single-cell RNA sequencing preparation and analysis

Freshly harvested tissues were washed in ice-cold RPMI 1640 and enzymatically dissociated using the Miltenyi Biotec's Multi-Tissue Dissociation Kit 2 per manufacturer specifications, with DNase treatment applied selectively based on homogenate viscosity. Following erythrocyte depletion (Miltenyi 130-094-183) and optional removal of cellular debris/dead cells (Miltenyi 130-109-398/130-090-101), cell counts and viability were quantified via fluorescence-based analysis (Countstar® Rigel S2) using acridine orange/propidium iodide dual staining. Viable cells underwent two washes in RPMI 1640 before resuspension at 1×10^6 cells/mL in PBS containing 0.04% bovine serum albumin. Single-cell RNA sequencing libraries were constructed with the SeekOne® Digital Droplet Single Cell 3' Library Kit, where preprocessed cells were mixed with reverse transcription master mix and loaded into a SeekOne® DD Chip S3 alongside hydrogel beads and partitioning oil. Reverse transcription in generated emulsion droplets proceeded at 42 °C for 90 min, followed by enzymatic inactivation at 80 °C for 15 min. cDNA was subsequently recovered, PCR-amplified, then fragmented, end-repaired, A-tailed, and adapter-ligated. Indexed PCR enriched DNA templates containing 3' poly-A regions, cell barcodes, and unique molecular identifiers. Final libraries were purified (SPRI beads), quantified via qPCR (KAPA Biosystems KK4824), and sequenced on Illumina NovaSeq 6000 (PE150) or DNBSEQ-T7 (PE100) platforms. All bioinformatic processing and analysis were performed using SeekSoul Tools software.

RNA extraction and RT-qPCR

Total RNA was extracted using Trizol kit (Sevenbiotech, Beijing, China) according to the manufacturer's instructions. RNA concentration and purity were measured using a Nano-2000 microspectrophotometer. Complementary DNA (cDNA) was synthesized from the extracted RNA using a reverse transcription kit (Vazyme, Nanjing, Jiangsu, China) in accordance with the

manufacturer's instructions. RT-qPCR was performed using SYBR Green qPCR Supermix (Vazyme) on an LC96 PCR system (Roche, Basel, Switzerland) with GAPDH as the reference control gene. Gene expression levels were calculated using the $2^{-\Delta\Delta}$Ct method. The reactions were run in triplicate, and detailed qPCR primer sequences are listed in Table S2. The thermal cycling conditions were as follows: initial denaturation at 95 °C for 30 s, followed by 40 cycles of denaturation at 95 °C for 10 s and annealing/extension at 60 °C for 30 s. Melting curve analysis was carried out from 60 to 95 °C to verify amplification specificity.

Western blot analysis

Protein extracts were resolved via 4–20% SDS-PAGE, followed by transfer onto PVDF membranes. The membranes were then probed with primary antibodies. A peroxidase-conjugated anti-mouse or anti-rabbit antibody served as the secondary antibody, and the ensuing antigen–antibody interaction was visualized using an enhanced chemiluminescence assay. Detailed information on antibodies can be found in Table S3.

Immunohistochemistry

Tissues were fixed in formalin, embedded in paraffin, andsectioned at a thickness of 3 μm thickness. For paraffin sections, antigen retrieval was performed either by heat-induced epitope retrieval or by proteinase K digestion, while this step is omitted for frozen sections. To minimize background staining, slides were blocked with 1–5% BSA for 1 h at room temperature. Primary antibodies, diluted at a ratio of 1:100–1:500, are incubated either overnight at 4 °C or for 2 h at room temperature. After that, HRP-conjugated anti-mouse or anti-rabbit igG secondary antibodies were applied for 1 h at room temperature, according to the host species of the primary antibody. Subsequently, DAB chromogenic detection (lasting 5 min) and hematoxylin counterstaining are conducted, followed by dehydration and mounting of the sections. Brown staining signals were evaluated under a light microscope for their distribution and intensity. Detailed antibodies information can be found in Table S3.

Atomic force microscopy measurements

Atomic force microscopy (AFM) measurements were conducted using an MFP3D AFM (Asylum Research, London, UK), followed previously established protocols [22]. Briefly, for PDAC tissues, frozen tissue sections of PDAC, 20 μm thick, were prepared. Prior to measurement, tissue sections or cells were immersed in PBS. During AFM examination, the samples were maintained in PBS containing a protease inhibitor and placed in an acoustic isolation enclosure for scanning. A borosilicate glass spherical probe with a diameter of 5 μm mounted on a silicon nitride cantilever with a spring constant of 0.06 N/m was used for measurement. Before each experiment, the cantilever was calibrated using the thermal oscillation method. For morphological imaging of tissues/cells, a scan matrix of 256 × 256 was applied. For AFM mechanical mapping, a scan area of 16 μm × 16 μm was used. The Hertz model was employed to calculate the elastic modulus (E1) of tissues and cells. The samples were assumed to be incompressible, and then a Poisson's ratio of 0.5 was used for the Young's modulus calculation. For each tissue sample, measurements were taken at three different positions, and the results were averaged.

Scanning electron microscopy

Cells were seeded on sterile coverslips in culture dishes and fixed prior to SEM processing. After cell collection, the culture dishes were stored at 4 °C. Tissue blocks were washed three times with 0.1 M phosphate buffer (PB, pH 7.4) for 15 min each, then transferred to 0.1 M PB (pH 7.4) containing 1% osmium tetroxide and incubated at room temperature for 1–2 h; afterwards, they were washed again 3 times with 0.1 M PB (pH 7.4), 15 min each time, followed by photographing.

Animal experiments

Six-week-old female BALB/c nude mice were used in this study. To establish the xenograft model, PDAC cells co-cultured with CAFs (shITGB5 or shNC) were subcutaneously injected into the right flank of mice. Tumor volume was calculated as short diameter^2 × long diameter/^{2}. Mice were divided into two experimental groups. In group A, tumor growth rate and weight were measured, and IHC was performed on harvested tumor tissues. In Group B, mice underwent MRI or MRE scanning when tumor volume reached ~ 1000 mm^3 (to minimize stiffness measurement bias), followed by euthanasia.

LSL-K-ras G12D (KI/+), LSL-Trp53 R172H (KI/+), and Pdx1-Cre (TG/+) (KPC) mice were purchased from Cyagen Biotechnology Co., Ltd. (Suzhou, China). The KrasLSL-G12D/+ and Pdx1-Cre mouse strains were initially bred with Trp53flox/flox mice. After two successive generations of breeding, F1 progeny carrying the KrasLSL-G12D/+; Trp53flox/flox genotype and those with the Pdx1-Cre; Trp53flox/flox genotype were intercrossed to generate triple-genotype KPC mice.

At 10–12 weeks of age, KPC mice were examined for palpable tumors—according to the experimental protocol, the tumors typically measured 4–5 mm in diameter, corresponding to the late pancreatic intraepithelial neoplasia/early tumor stage. After two independent researchers confirmed the presence of tumors for two consecutive days, the mice were randomly divided into two cohorts: the first cohort (15 KPC mice per treatment group) was

desighated for survival analysis. The second cohort (5 KPC per treatment group) was used for histopathological analysis.The first group (control group) received intraperitoneal injections of an equivalent volume of 0.9% saline (vehicle) twice a week. The second group (gemcitabine group) was treated with intraperitoneal injections of gemcitabine at a dose of 50 mg/kg twice a week. The third group (cilengitide group) received cilengitide via tail vein injection at a dose of 30 mg/kg once every three days. The fourth group (gemcitabine plus cilengitide group) was administered gemcitabine (25 mg/kg twice a week) in combination with cilengitide via tail vein injection (15 mg/kg once every three days). For the histopathology cohort, treatment was discontinued 4 weeks after the initiation, and animals were euthanized. For the survival cohort: mice were monitored until they reached the experimental endpoint. Humane endpoints were defined as signs of advanced pancreatic cancer, including abdominal distension, cachexia-like deterioration, reduced mobility, ascites, overnight weight loss > 10% or total weight loss ≥ 20% of maximum body weight, hunched posture, signs of distress, or tumor burden interfering with mobility or food/water access. Maximum tumor burden permitted by ethical approval was not exceeded. Mice reaching endpoints prematurely due to non-tumor-related causes were censored.

MRE imaging and data processing

MRE acquisition and data processing were performed as previously described [21, 23]. Before imaging, water was withheld from the for 6 h. Anesthesia was induced and maintained with 1.5% isoflurane during scanning. Mice were positioned laterally within a custom-made, eight-channel small-animal magnetic resonance coil (5-cm inner diameter; Suzhou Medcoil Healthcare Co., Ltd.). A hemispherical aerodynamic mechanical wave transducer was placed in close contact with the tumor to deliver 200 Hz vibrations during MRE.

CCK-8 assay

Cell viability was assessed using a CCK-8 assay (Dojindo, Japan) according to the manufacturer's instructions. Cells were seeded at 2×10^3 cells per well in 96-well plates. At designated time points, 10 μL of CCK-8 reagent was added to each well, and plated were incubated per the manufacture's protocol. Absorbance at 490 nm was measured using a Varioskan Flash microplate reader (Thermo Fisher Scientific).

Colony formation assay

PDAC cells co-cultured with CAFs from the indicated experimental groups were seeded into 6-well plates. After 2 weeks of incubation, colonies were fixed in 4% formaldehyde and stained with 0.5% crystal violet. Colonies were imaged using a digital camera (Olympus, Tokyo, Japan).

Transwell assay

For each Transwell insert, 200 μL of PDAC cell suspension a containing 3×10^4 cells was added to the upper chamber. The lower chamber was filled with 600 μL of culture medium supplemented with. After 24 h, cells that had migrated to the lower surface of the membrane were fixed with 4% paraformaldehyde and stained with 0.5% crystal violet. Invaded cells were counted under aa Nikon microscope.

EdU

The EdU assay was used to assess cell proliferation in PDAC cells. Cells were incubated with 20 μM EdU for 2 h. Cells were then fixed with paraformaldehyde and nuclei were counterstained with DAPI. The percentage of EdU-positive cells was quantified.

Bioinformatics analysis

Transcriptomic data and tumor mutation burden (TMB) data for PDAC patients were obtained from The Cancer Genome Atlas (TCGA), andtranscriptomic data for 63 pancreatic cancer patients were retrieved from GEO (accession GSE57495). Allanalyses were performed in R (version 4.0.5). Cancer-associated fibroblast (CAF) infiltration in the both TCGA and GEO cohorts was estimated using four algorithms (EPIC, TIDE, MCP-counter, and xCell) and a stromal score was calculated to quantify stromal infiltration. Survival was assessed by the Kaplan–Meier method and group differences tested with the log-rank test. Weighted gene co-expression network analysis (WGCNA) was used to identify co-expressed gene module the module showing the strongest positive correlation with CAF infiltration and stromal score was selected. Overlapping genes between the TCGA- and GEO-derived modules were identified (Venn diagram) and subjected to KEGG and GO enrichment analyses. Prognosis-related genes in PAAD were screened by univariate Cox regression and refined by LASSO to define core genes. A risk score based on core-genes expression was used to dichotomize patients at the median into high- and low-risk groups; receiver operating characteristic ROC curves evaluated predictive performance. Spearman correlation analysis assessed relationships between core genes and pro-stromal genes. Immunotherapy response in the risk groups was predicted using TIDE. Finally, mutational landscapes for the risk groups were computed and visualized using the R package maftools.

Statistical analysis

Cntinuous variables with an approximately normal distributionare reported as mean ± standard deviation (SD),

non-normally distributed continuous variables are presented as medians. Categorical variables are summarized as countss and percentages unless otherwise specified. Fortwo groups comparisons,Student's t-tes was used for normally distributed continuous variables and the Mann–Whitney U test for non-normal data. Normality was assessed using the Shapiro–Wilk test. Comparisons among three or more groups were performed with one-way ANOVA (Tukey's post hoc test) for parametric data or the Kruskal-Walli's test (Dunn's post hoc test) for non-parametric data. Categorical variables were compared using the chi-squared test (χ^2 test) or Fisher's exact test when expected cell counts were < 5. Survival curves are generated by the Kaplan–Meier method and compared using the log-rank test. All statistical analyses and figures were produced using R (version 4.0.5) and GraphPad Prism (version 10.2.1). All tests were two-sided, and $p < 0.05$ was considered statistically significant.

Results

Infiltration of CAFs mediates stromal stiffening and poor prognosis in PDAC

In this prospective clinical trial, 80 patients with PDAC underwent conventional magnetic resonance imaging (MRI) and magnetic resonance elastography (MRE) (Table S1). T2FS images did not distinguish biomechanical differences between tumors, whereas MRE detected marked biomechanical heterogeneity (Fig. 1A, B, the first row). Using the median MRE shear stiffness at 40 Hz (median = 2.3), patients were dichotomized PDAC patients into high-stiffness (HS) and low-stiffness (LS) groups (Fig. 1E, HS vs. LS, $p < 0.0001$). The HS group showed increased collagen deposition (Fig. 1A–B, second row; Fig. 1F, $p < 0.0001$) and elevated expression of the activated CAF marker α-SMA (Fig. 1A–B, third row; Fig. 1G, $p < 0.0001$). Ki-67 immunostaining was also higher in the HS group, indicating greater tumor cell proliferation (Fig. 1A, B, the fourth row, and Fig. 1H, HS vs. LS, $p < 0.0001$). Furthermore, Collagen deposition correlated strongly with stromal shear stiffness (Fig. 1J, r = 0.795, $p < 0.0001$). Atomic force microscopy (AFM) on the same tissue sections corroborated the MRE findings: the HS group exhibited a significantly higher Young's modulus and pronounced surface irregularity on 2D/3D deflection-retrace topographies (Fig. 1C–D; HS vs. LS, $p < 0.0001$). In independent transcriptomic cohorts (TCGA-PAAD and GSE57495), higher estimated CAF infiltration was associated with worse survival in multiple algorithms In TCGA-PAAD by EPIC (HR = 4.363, 95% CI 1.589–11.977, $p = 0.02$) and MCP-counter (HR = 2.905, 95% CI 1.260–6.699, $p = 0.009$) (Fig. 1K–L), and in GSE57495 by MCP-counter (HR 2.37, 95% CI 1.074–5.229, $p = 0.028$) and TIDE (HR = 2.169, 95% CI 1.147–4.102, $p = 0.015$) (Fig. 1M–N). In conclusion, these data indicate CAF activation and collagen accumulation contribute to stromal stiffening in PDAC and that increased CAF infiltration is associated with poorer prognosis. Identifying genes that regulate CAF infiltration may therefore reveal candidate therapeutic targets for this aggressive malignancy.

Identification of core genes mediating CAFs infiltration by weighted gene co-expression network analysis

Using WGCNA, we identified co-expressed gene modules in both TCGA-PAAD and GSE57495 cohorts. In TCGA, the blue module was strongly correlated with estimated CAF infiltration (Fig. 2A, r = 0.76, $p = 2e^{-34}$; r = 0.8, $p = 3e^{-40}$). In GSE57495, the green module correlated with CAF infiltration and stromal score (Fig. 2B; r = 0.81 , $p = 2e^{-50}$; r = 0.64, $p = 2e^{-26}$). Intersection of these modules yielded 120 overlapping genes (Fig. 2C) which were enriched for pathways implicated in stromal remodeling and fibrosis, including the *PI3K-AKT* signaling pathway (Fig. 2D, E). Univariate COX regression identified 34 prognosis-associated, high-risk genes, including *ITGB5* (all $p < 0.01$, Fig. 2F). LASSO regression further prioritized six core genes (*ANTXR2*, *ITGB5*, *ANXA1*, *BCAT1*, *PLAU* and*TGFB1*) most predictive of outcome (Fig. 2G). Patients were dichotomized at the median expression of the core-gene signature into high- and low-risk groups; the resulting model demonstrated good discriminative performance (Fig. 2H, AUC: 0.756, 95% CI 0.678–0.828). High-risk patients had significantly worse survival in TCGA (Fig. 2I, $p = 0.025$; HR 1.596, 95% CI 1.055–2.412) and GSE57495 (Fig. 2J, $p < 0.001$; HR 3.321, 95% CI 1.729–6.379). These findings nominate *ANTXR2*, *ITGB5*, *ANXA1*, *BCAT1*, *PLAU*, and *TGFB1* as candidate regulators of CAF infiltration and potential targets for stroma-directed therapies in PDAC.

Hub genes mediate CAFs infiltration and attenuate immune response in the PDAC

To validate the robustness of the CAF signature as a predictor of CAF infiltration, we computed Spearman's rank correlation between the CAF risk score and stromal scores, as well as CAF abundance estimated by EPIC, xCell, MCP-counter and TIDE. In the TCGA-PAAD cohort (Fig. 3A), the CAF risk score correlated strongly and positively with CAF abundance across multiple estimation methods and with stromal scores. Moreover, within the TCGA-PAAD (Fig. 3B–C), both the CAF risk score and the expression levels of the six core genes were positively associated correlations with a panel of established CAF markers. Using the TIDE algorithm to evaluate predicted response to immune checkpoint blockade, only 22% of patients in the high-risk group were predicted to respond, compared with 57% in the low-risk group (Fig. 3D–E, all $p < 0.001$). This suggests

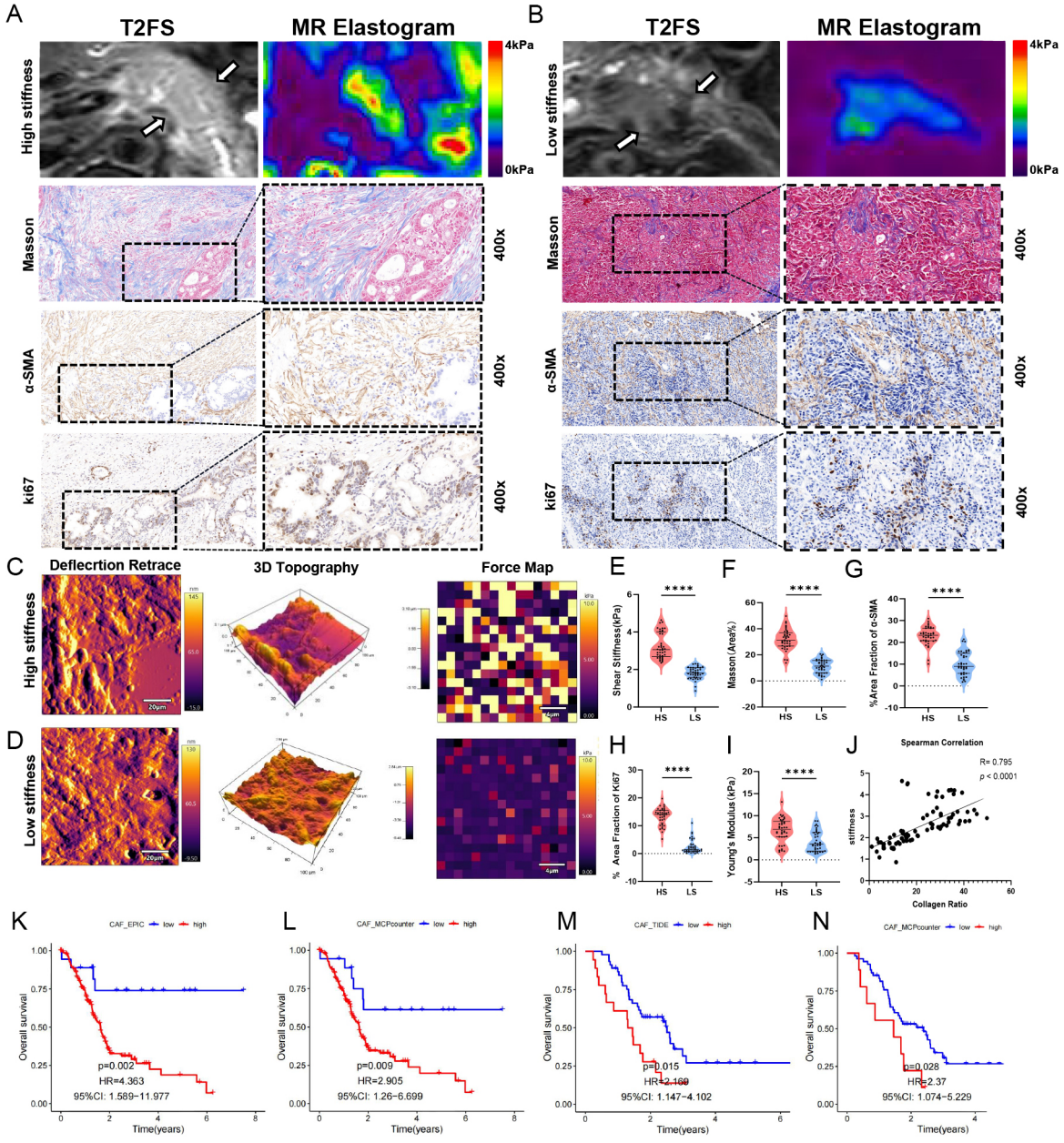


Fig. 1 CAFs infiltration and collagen fiber deposition drive stromal stiffening and are associated with poor prognosis in PDAC. **A**–**B** Representative T2FS images, MR elastography maps, Masson's trichrome staining, and immunohistochemistry for *a-SMA* and Ki67 in tumors from HS and LS groups. **C**–**D** Representative AFM images from high-HS and LS tumors, including deflection-retrace maps, 3D topography, and force curves. **E** Violin plot of MRE shear stiffness (40 Hz) in HS versus LS groups. **F** Violin plot of collagen deposition. **G** Violin plot of *a-SMA* expression. **H** Violin plot of *Ki-67* expression. **I** Violin plot of Young's modulus. **J** Spearman correlation between collagen deposition and tumor shear stiffness. **K**–**L** Kaplan–Meier survival curves comparing patients stratified by estimated CAF infiltration in TCGA-PAAD (CAF estimates derived from immune-infiltration algorithms). **M**–**N** Using immune infiltration algorithms to calculate the association between CAF infiltration levels and prognosis in PDAC patients from the GEO database, and visualizing the prognostic differences with Kaplan–Meier (KM) curves. Violin plots indicate the distribution and density of the data. The central dashed line denotes the median, and the upper and lower dashed lines indicate the 25th and 75th percentiles, respectively. Statistical significance between Kaplan–Meier curves was assessed using a two-sided log-rank test. A *p*-value < 0.05 was considered statistically significant

that low-risk patients are less likely to undergo immune escape and more likely to benefit from immunotherapy. In addition, high-risk patients exhibited higher frequencies of mutations in commonly altered PDAC genes than low-risk patients (*KRAS*: 72% vs. 51%; *TP53*: 69% vs.43%; *SMAD4*: 25% vs.19%; *CDKN2A*: 21% vs. 14%), indicating an association between the hub-gene signature, the PDAC mutational landscape, and the tumor microenvironment. Collectively, these findings suggest that hub-gene signature predicts CAF abundance, correlates with

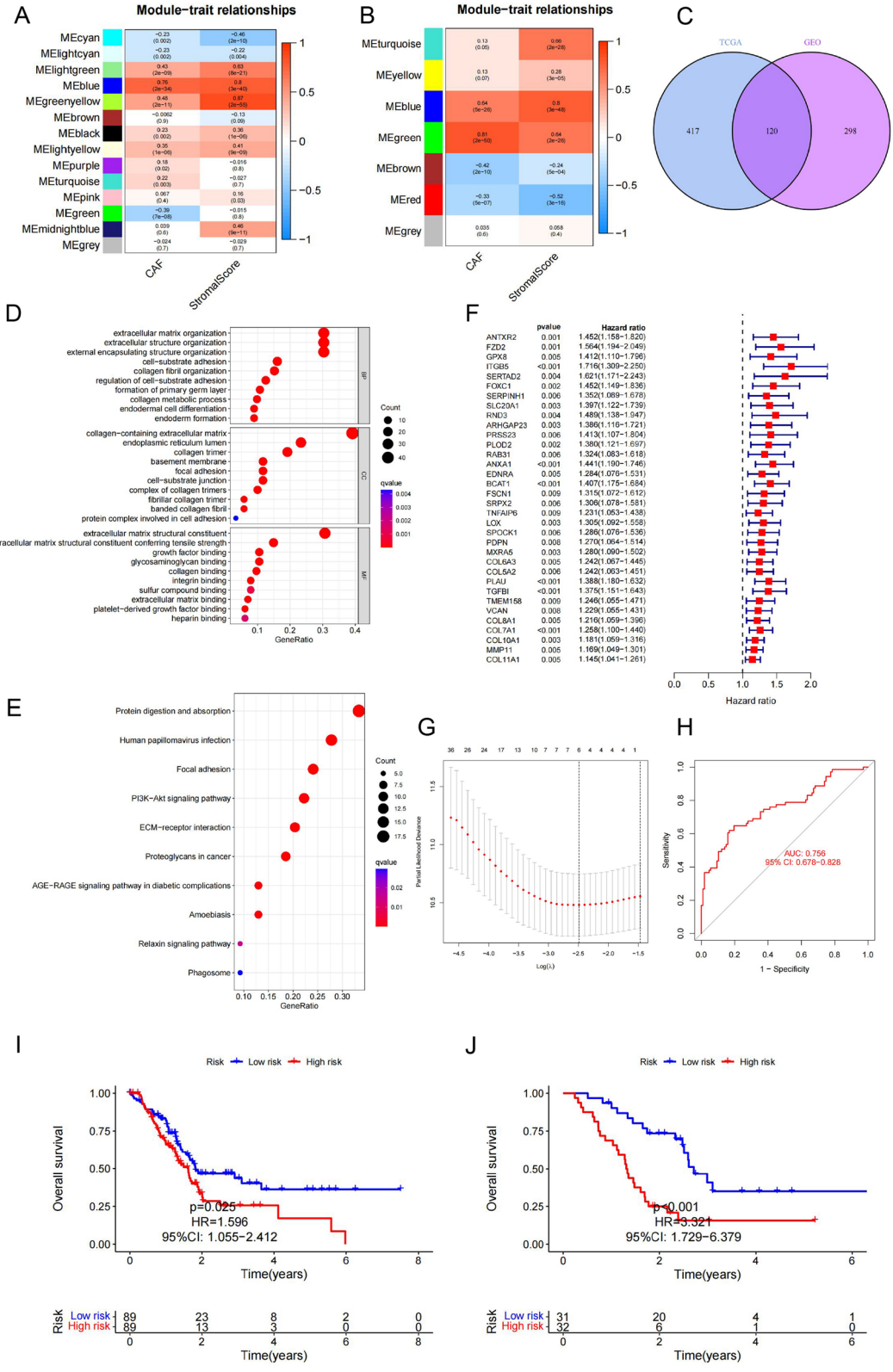


Fig. 2 (See legend on next page.)

(See figure on previous page.)

Fig. 2 Identification of hub genes mediating CAF infiltration. **A**–**B** WGCNA results showing module-trait relationships in PDAC patients from TCGA-PAAD (**A**) and GSE57495 (**B**). **C** Venn diagram of overlapping genes between the selected TCGA and GEO modules. **D**–**E** Functional enrichment of intersecting genes by Gene Ontology (GO; biological processes) and KEGG pathway analysis, respectively. **F** Univariate Cox regression assessing associations between intersecting genes and overall survival. **G** LASSO regression used to derive a multi-gene prognostic signature. **H** Receiver operating characteristic (ROC) curve evaluating the predictive performance of the prognostic signature. **I**–**J** Kaplan–Meier survival curves comparing high- and low-risk PDAC patients in TCGA-PAAD (**I**) and GSE57495 (**J**). Statistical significance between Kaplan–Meier curves was assessed using a two-sided log-rank test. A p-value < 0.05 was considered statistically significant

the immunotherapy response predicted by TIDE, and reflects differences in PDAC mutational profiles. Analysis of the Cancer Cell Line Encyclopedia (CCLE) showed that *ANTXR2, ITGB5, BCAT1*, and *TGFB1* were enriched in fibroblast lines but not in PDAC cell lines (Fig. 3H–I; all $p < 0.05$). *ANXA1* did not show significant enrichment, whereas *PLAU* was predominantly expressed in PDAC cells.

ITGB5 is highly expressed in CAFs from high-stiffness PDAC tissues

To identify candidate therapeutic targets, we performed single-cell RNA sequencing on tumor specimens from eight PDAC patients, four classified as high-stiffness (HS) group and four as low-stiffness (LS) group. Follwing quality control, UMAP dimensionality reduction revealed 16 cell clusters (Fig. 4A). Using canonical marker genes (Fig. 4D), we annotated 12 distinct cell types, including a fibroblast cluster (Fig. 4B–C). We next projected expression of *ITGB5*, *TGFB1*, *ANTXR2*, and *BCAT1* onto the UMAP embedding to determine their cellular localization. Only *ITGB5* showed high expression sepcifically in CAFs (Fig. 4E), and ITGB5 expression in CAFs was markedly higher in HS versus LS samples (F4g. 4I, HS vs. LS, $p < 2.22e^{-16}$).*TGFB1* and *BCAT1* were also upregulated in HS samples (Fig. 4J–K, HS vs. LS, $p < 2.22e^{-16}$), but *TGFB1* localized primarily to T & NK cells (Fig. 4F), consistent with a possible indirect role in modulating CAF infiltration via intercellular signling. *ANTXR2* was also enriched in CAFs, but showed significantly higher abundance in HS versus LS samples (Fig. 4L, LS vs. HS, $p = 1.6e^{-12}$).

We performed univariate and multivariate Cox regression analyses for these four genes. For overall survival (OS), univariate analysis associated high *ITGB5, ANTXR2*, and *BCAT1* expression with shorter OS (Table S5, Univariate analysis, all $p < 0.05$), whereas *TGFB1* exprssion remained an independent predictor of worse OS (Table S5, Multivariate analysis, $p = 0.033$), whereas *ANTXR2* and *BCAT1* did not. For progression-free interval (PFI), univariate analysis linked high *ITGB5* and *BCAT1* expression to shorter PFI (Table S6, Univariate analysis, all $p < 0.05$), but in multivariate models only *ITGB5* remained significantly associated with shorter PFI (Table S6; multivariate $p = 0.005$).

Together, these results identify *ITGB5* as a robust candidate CAF-associated therapeutic target in PDAC: *ITGB5* is specifically overexpressed in CAFs from high-stiffness tumors and is independently associated with poorer OS and PFI. While this supports prioritizing *ITGB5* for further functional validation, experimental studies are required to determine whether targeting *ITGB5* will suppress CAF function and alter PDAC progression.

Matrix stiffness enhances cell–cell communication and alters cell fate

Using single-cell RNA sequencing integrated with MRE measurements, the proportion of fibroblasts was similar between the HS and LS cohorts (Fig. 5A–B, HS: 8.83%, LS: 7.82%). These data suggests that PDAC stiffness may be independent of CAF abundance and instead determined by CAF functionality states. To test this hypothesis, we performed cell–cell communication analysis across the eight samples. Both the frequency and inferred strength of intercellular signaling were higher in HS than LS samples (Fig. 5C–D).

In HS samples we observed increased activity of signaling axes including *TIGIT, CD6, ALCAM*, and *FN1*, pathways broadly implicated in immune suppression and extracellular matrix (ECM) remodeling/stiffening. By contrast, LS samples were enriched for signaling pathways such as *PSAP*, *TENASCIN*, *TNF*, *TRAIL*, *CLDN*, and *IL-6*, which are more closely associated with tumor cell malignancy and inflammatory responses (Fig. 5E).

Differences in stromal stiffness were also associated with distinct cell-state trajectories. Pseudotime trajectory analysis mapped developmental landscapes in HS and LS groups, and revealed three major branches (Fig. 5F–G). Notably, cells from the HS samples were preferentially localized to branch 1 (pre-branch) and branch 2. Of the core genes *TGFB1*, *ANTXR2*, *BCAT1*, and *ITGB5*, only *ITGB5* was preferentially enriched in branch 1 (Fig. S1A). Pseudotime analysis of CAF subpopulations revealed that branch 1 overlapped with trajectories of multiple CAF subtypes, including myofibroblastic CAFs (mCAFs) and inflammatory CAFs (iCAFs) (F5g. 5I), supporting a specific association of ITGB5 with CAFs and their subtypes.

Heatmap-based clustering identified four gene co-expression clusters (Fig. 5J; Table S4). ITGB5 expression was largely confined to Cluster 3, in contrast to *TGFB1, ANTXR2,* and *BCAT1*. GO and KEGG enrichment analysis indicated that Cluster 3 is primarily involved in ECM remodeling (Fig. S1D), whereas Clusters 1, 2, and 4 are

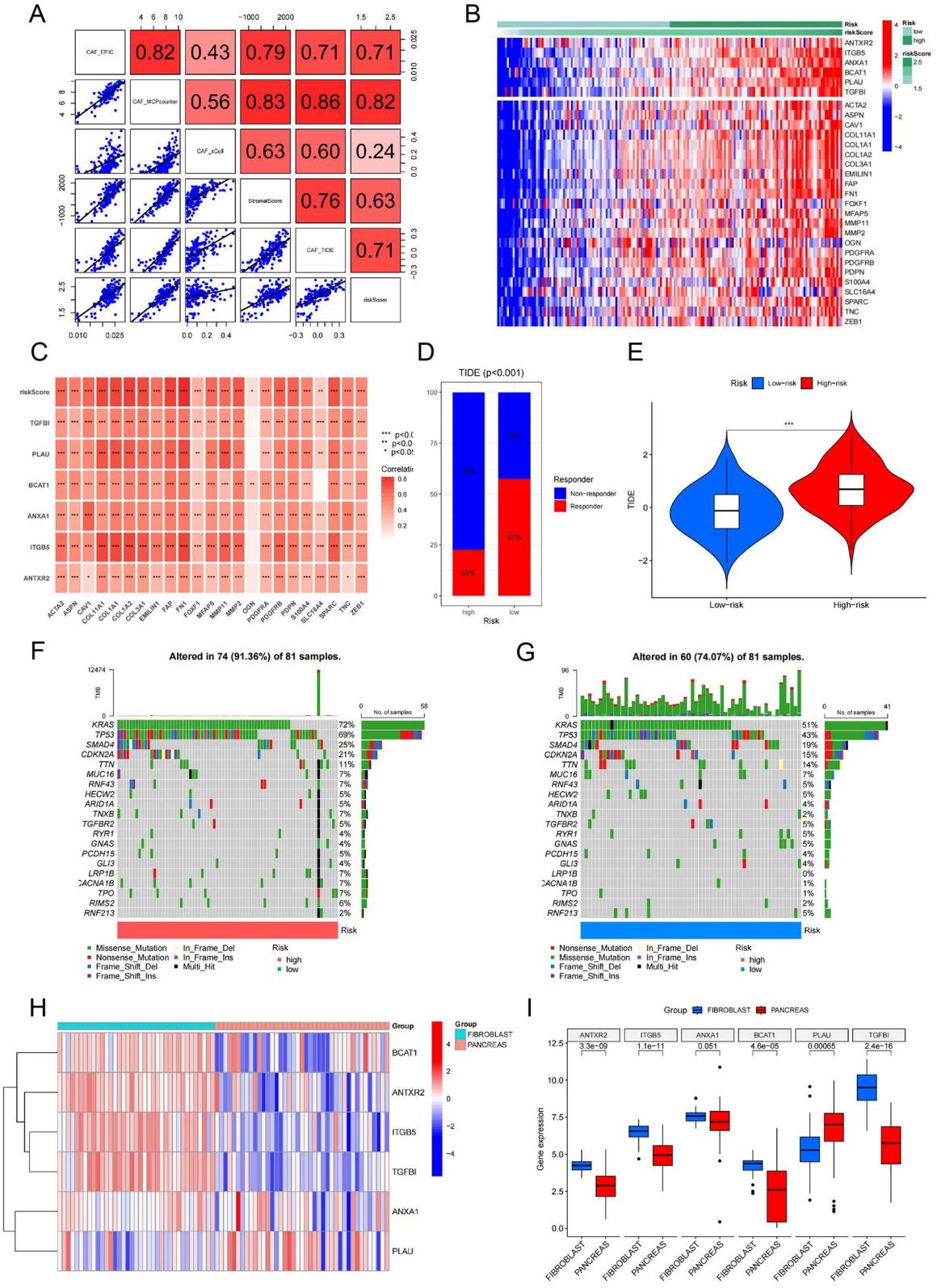


Fig. 3 (See legend on next page.)

(See figure on previous page.)

Fig. 3 The hub-gene signature predicts CAFs abundance, immunotherapy response, and the mutational landscape in PDAC. **A** Spearman correlation analysis between the CAF risk score, stromal score, and CAF abundance estimated by multiple algorithms (EPIC, xCell, MCP-counter, TIDE). **B** Heatmap showing correlations between the six hub genes and the CAF risk score. **C** Correlation analysis between the six hub genes and established CAF markers. **D**–**E** Predicted responses to immune checkpoint blockade in high- and low-risk groups as assessed by the TIDE algorithm (predicted responder vs. non-responder). **F**–**G** Waterfall/oncoplot visualizations of the somatic mutation landscape in high- and low-risk PDAC patients. **H**–**I** Analysis of cell-type enrichment for hub-gene expression using the Cancer Cell Line Encyclopedia (CCLE). Spearman's rank correlation was used for associations between continuous variables, with r denoting the correlation coefficient. Violin plots (where shown) display data density; the central dashed line denotes the median, and the upper and lower dashed lines indicate the 25th and 75th percentiles, respectively. Spearman's rank correlation analysis was performed to assess the association between continuous variables, with *r* representing the correlation coefficient. Violin plots indicate the distribution and density of the data. The central dashed black line within each violin represents the median, and the upper and lower dashed lines indicate the 25th and 75th percentiles, respectively. A *p*-value < 0.05 was considered statistically significant

enriched for processes related to immune infiltration, cytokine signaling, and inflammatory responses (Fig. S1B–C, E).

High ITGB5 expression in CAFs promotes malignant phenotypes of PDAC cells

Based on single-cell RNA sequencing data, *ITGB5* was selected for further functional validation. We generated stable *ITGB5*-knockdown CAF lines by lentiviral transduction of two independent shRNAs (shRNA#1 and shRNA#2). qPCR confirmed efficient *ITGB5* expression knockdown by both shRNAs relative to shNC (Fig. 6A, all $p < 0.0001$).

To test whether CAF *ITGB5* modulates PDAC cell behaviour, conditioned media (CM) were collected from shNC and *ITGB5*-knockdown (sh*ITGB5*) CAFs, and applied to PDAC cells. Colony formation assays showed that CM from *ITGB5*-knockdown CAFs significantly reduced PDAC clonogenicity compared with CM from shNC CAFs. Transwell assays revealed that CM from *ITGB5*-knockdown CAFs reduced PDAC cell migration and invasion (Fig. 6C, $p < 0.05$).

Co-culture of PDAC cell lines (CFPAC-1 and Mia-PaCa-2) with *ITGB5*-knockdown CAFs reduced tumor-cell proliferation as measured by EdU incorporation (Fig. 6D–E; for CFPAC-1: CAFs-shNC vs. CAFs-shRNA#1 and CAFs-shRNA#2, $p < 0.01$; for Mia Paca-2: CAFs-shNC vs. CAFs-shRNA#1 and CAFs-shRNA#2, $p < 0.001$).

CCK-8 assays showed reduced PDAC cell viability at 48, 72, and 96 h following exposure to CM from *ITGB5*-knockdown CAFs (Fig. 6F–G, all $p < 0.05$). Atomic force microscopy showed that *ITGB5* -knockdown led to a significant decrease in CAF stiffness (Fig. 6H, shNC vs. shRNA, $p < 0.05$). Scanning electron microscopy further indicated that loss of *ITGB5* impaired the morphological stability of CAFs, characterized by retracted and reduced filopodia formation (Fig. 6I). Western blotting revealed decreased *COL1A1* and *α-SMA* protein levels in *ITGB5*-knockdown CAFs (Fig. 6J–L, all $p < 0.0001$).

Together, these data indicate that *ITGB5* suppression in CAFs attenuates PDAC cell malignant phenotypes, potentially via disruption of CAF biomechanical and matrix-producing functions. Further mechanistic studies are required to define the downstream pathways mediating these effects.

Suppressing ITGB5 inhibits PDAC progression and remodels tumor biomechanics in subcutaneous xenograft and KPC models

To further investigate the role of *ITGB5* in the biomechanics and progression of Pacwa used subcutaneous xenografts in nude mice and a genetically engineered KPC model. For xenografts, CFPAC-1 and Mia PaCa-2 cells were co-injected subcutaneously with *ITGB5*-knockdown or control CAFs at a 1:2 ratio into nude mice. MRE on size-matched tumors demonstrated that co-injection with *ITGB5*-knockdown CAFs significantly reduced tumor shear stiffness compared with controls (Fig. 7A–B, shNC vs. shRNA#2, all $p < 0.0001$). Immunohistochemical of subcutaneous tumors showed that *ITGB5* expression was markedly inhibited in the shRNA groups (Fig. 7C–D, the first two rows, shNC vs. shRNA#2, all $p < 0.01$). Similarly, the fibrosis marker *α-SMA* was significantly decreased in *ITGB5*-knockdown groups (Fig. 7C–D, the last two rows, shNC vs. shRNA#2, all $p < 0.001$). Tumor growth curves demonstrated that tumors in the *ITGB5*-knockdown groups grew more slowly and weighed less at endpoint (day 28) than controls (Fig. 7E–G, H–J, shNC vs. shRNA, all $p < 0.001$).

Although subcutaneous xenografts provide initial evidence that CAF *ITGB5* promotes tumor fibrosis and growth, they do not fully recapitulate the native PDAC microenvironment. Therefore, we employed a genetically engineered KPC mouse model in this study, assigning animals to the Vehicle, Gemcitabine, Cilengitide, and combination Gemcitabine + Cilengitide treatment groups. Immunohistochemistry in KPC tumours showed highes *ITGB5* expression in vehicle mice, reduced levels in single-agent groups, and the greatest suppression in the combination treatment (Fig. 7K–O, the first row, all $p < 0.01$). *α-SMA* staining was reduced across treatment groups, most prominently in the combination treatment (Fig. 7K–N, the second row, and Fig. 7P, all $p < 0.01$).

Notably, Gemcitabine treatment increased collagen fiber deposition relative to Vehicle, (consistent with

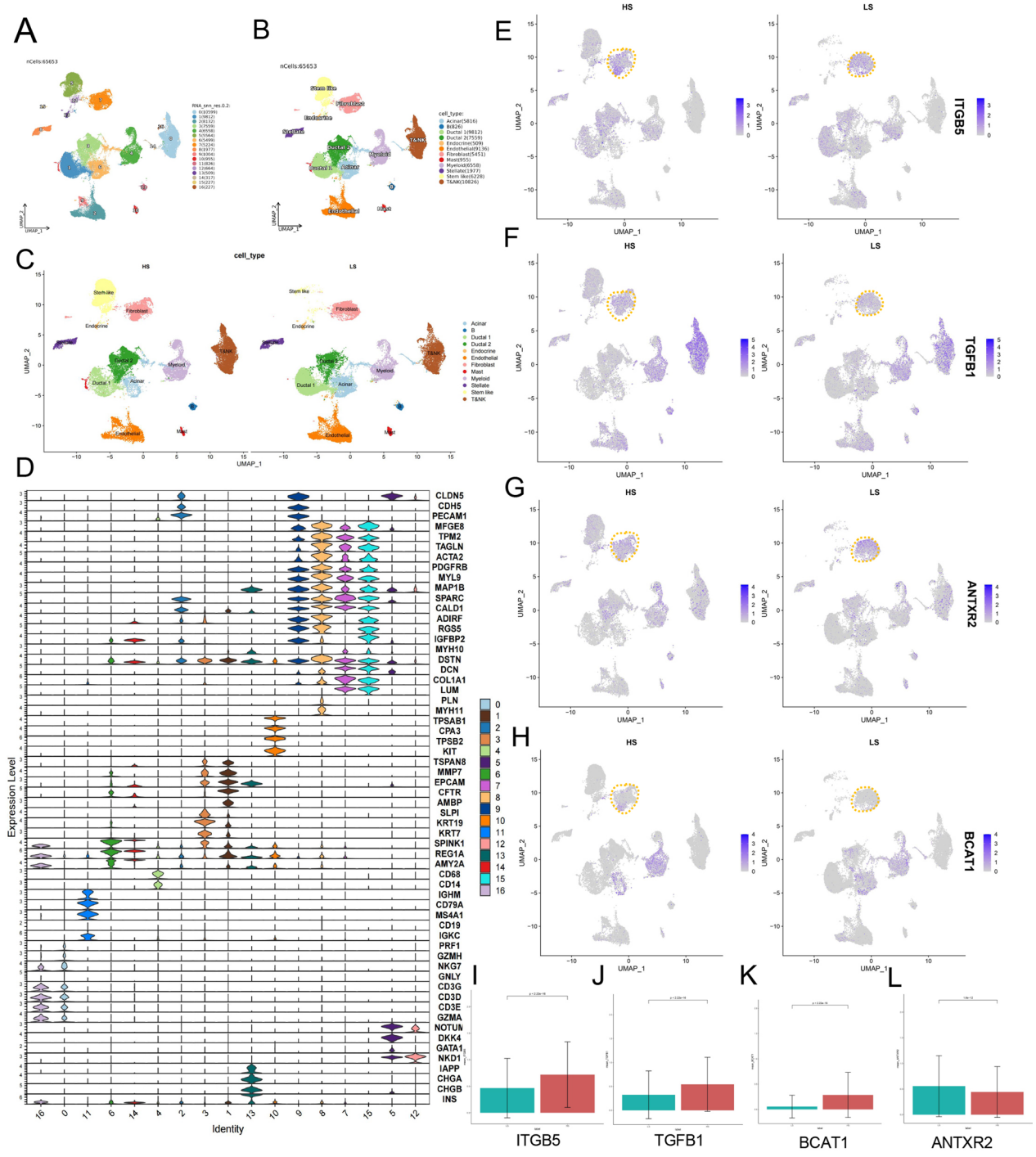


Fig. 4 Single-cell RNA sequencing reveals elevated ITGB5 expression in CAFs from high-stiffness PDAC. **A** Dimensionality reduction analysis of PDAC samples using UMAP. **B** Annotation of 16 cell clusters using UMAP. **C** Relative proportions of cell clusters in the high-stiffness and low-stiffness groups. **D** Violin plots of canonical marker genes used for cell-type annotation. **E**–**H** UMAP feature plots showing expression of *ITGB5*, *TGFB1*, *ANTXR2*, and *BCAT1* across cell clusters. **I**–**L** Boxplots comparing *ITGB5* (**I**), *TGFB1* (**J**), *ANTXR2* (**K**), and *BCAT1* (**L**) expression in fibroblasts between HS and LS groups; statistical comparisons performed by Wilcoxon rank-sum test, with p-values indicated. Statistical tests and significance thresholds are indicated in the figure; $p < 0.05$ was considered statistically significant

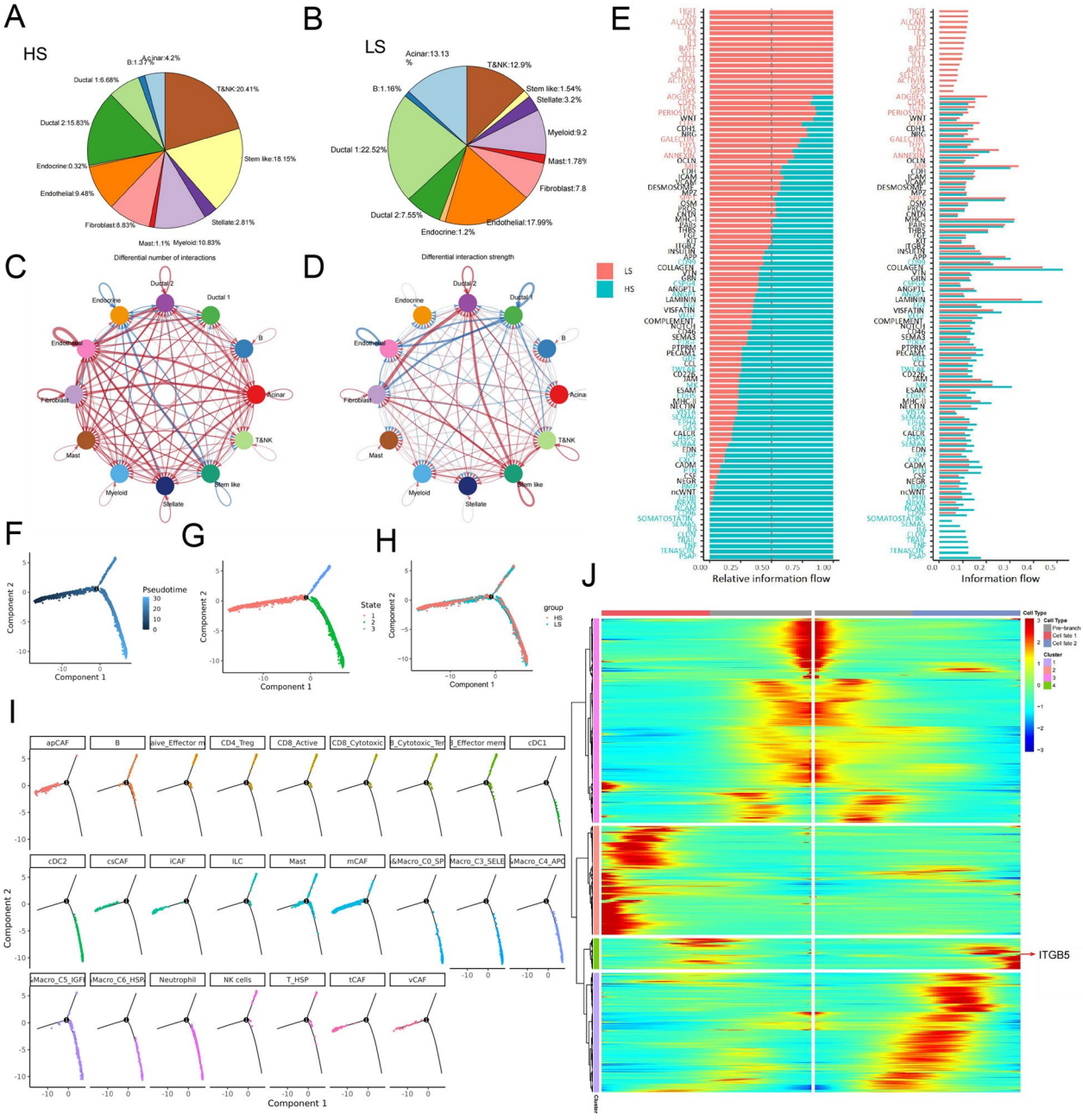


Fig. 5 Single-cell transcriptomic landscape of cell–cell communication and pseudotime trajectory differences between high-stiffness and low-stiffness PDAC. **A**–**B** Differences in cell population distribution between the HS and LS groups visualized using pie charts. **C**–**D** Differences in cell–cell communication strength between the HS and LS groups visualized using circle plots with red (or blue) color coding. **E** Bar chart displaying the ranking of key signaling pathways based on the differential overall information flow within the inferred network between HS and LS groups. **F**–**G** Trajectory reconstruction of all single cells reveals three branches: Branch 1 (pre-branch), Branch 2, and Branch 3, along with the distribution of HS and LS cells along each branch. Red indicates the HS group, and blue indicates the LS group. **I** Trajectory reconstruction of different cell subtypes to show their distribution across the various branches. **J** Gene expression heatmap of 1996 differentially expressed genes (DEGs) arranged in pseudotemporal order, categorized into four clusters. Clusters are indicated on the left, and cell types are shown at the top. Bar plots display expression levels. The red arrow marks the cluster containing ITGB5. Cell–cell communication inference was performed using CellPhone DB; differential pathway flow was computed as described in Methods. Statistical comparisons were performed using appropriate tests (e.g., Wilcoxon rank-sum or Fisher's exact test), and *p*-values or adjusted p-values are indicated where applicable

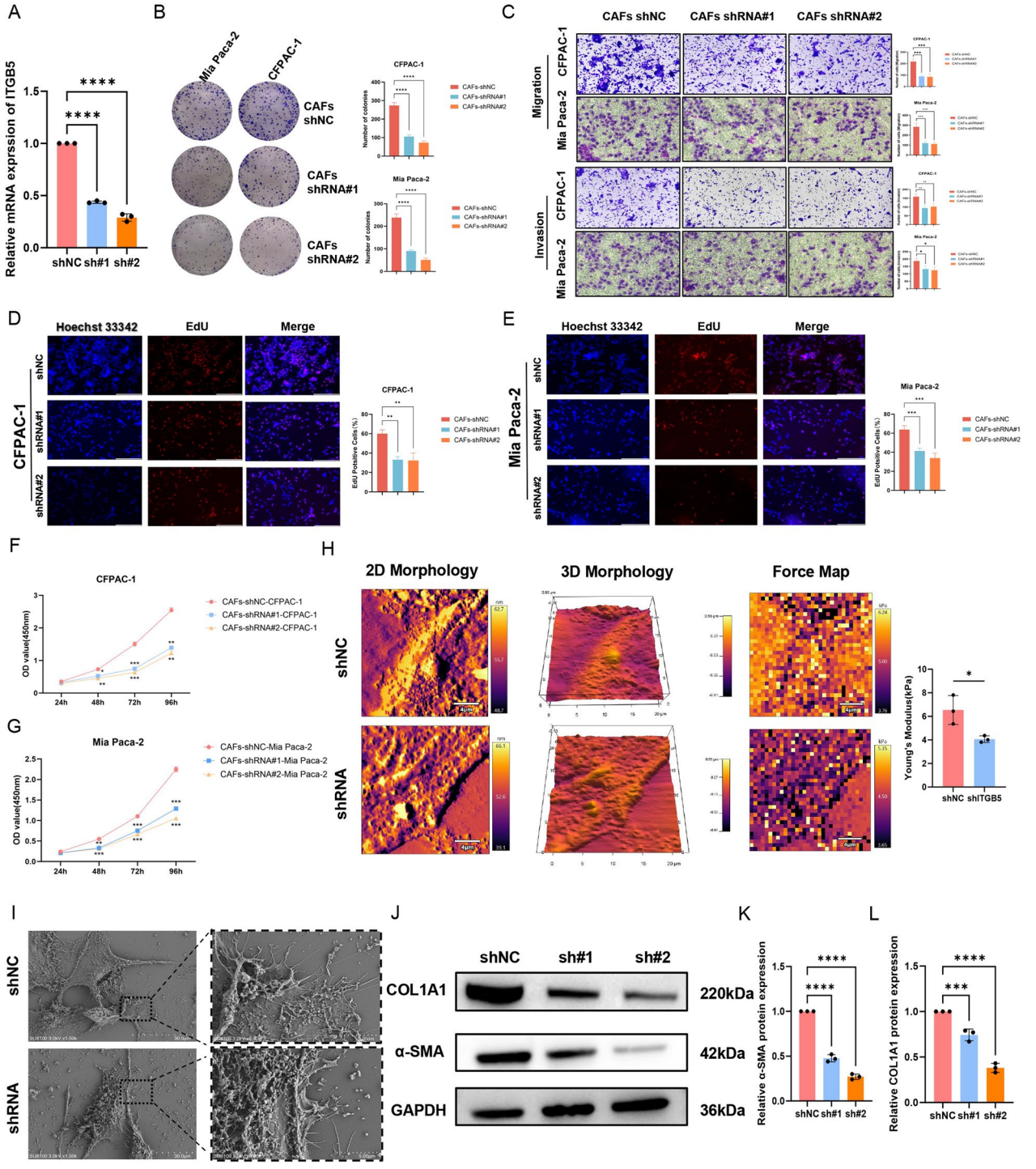


Fig. 6 *ITGB5* promotes malignant phenotypes and biomechanics of PDAC in vitro. **A** qPCR validation of *ITGB5*-knockdown efficiency in CAFs (two independent shRNAs: shRNA#1, shRNA#2; shNC = negative control). **B** Colony-formation assays assessing PDAC clonogenicity after treatment with conditioned media (CM) from control or *ITGB5*-knockdown CAFs. **C** Transwell migration and Matrigel invasion assays of PDAC cells exposed to CM from control or *ITGB5*-knockdown CAFs. **D**–**E** EdU incorporation assays showing PDAC cell proliferation following co-culture with control or *ITGB5*-knockdown CAFs. **F**–**G** CCK-8 cell viability assays at multiple time points (48, 72, 96 h) after exposure to CM from control or *ITGB5*-knockdown CAFs. **H** AFM characterization of CAF mechanical properties: comparison of Young's modulus between *ITGB5*-knockdown and control CAFs. **I** Representative scanning electron microscopy (SEM) images showing morphological changes in *ITGB5*-knockdown versus control CAFs. **J**–**L** Western blotting and quantification of fibrosis/CAF markers (e.g., *COL1A1*, *α-SMA*) in CAFs following *ITGB5*-knockdown. Data are presented as mean ± SD (indicate n for each experiment in the figure or legend). For comparisons between two groups, the Mann–Whitney U test was used; for comparisons among three groups, the Kruskal–Wallis test was applied (followed by appropriate post hoc testing where applicable). Statistical significance: *$p < 0.05$, **$p < 0.01$, ***$p < 0.001$, ****$p < 0.0001$

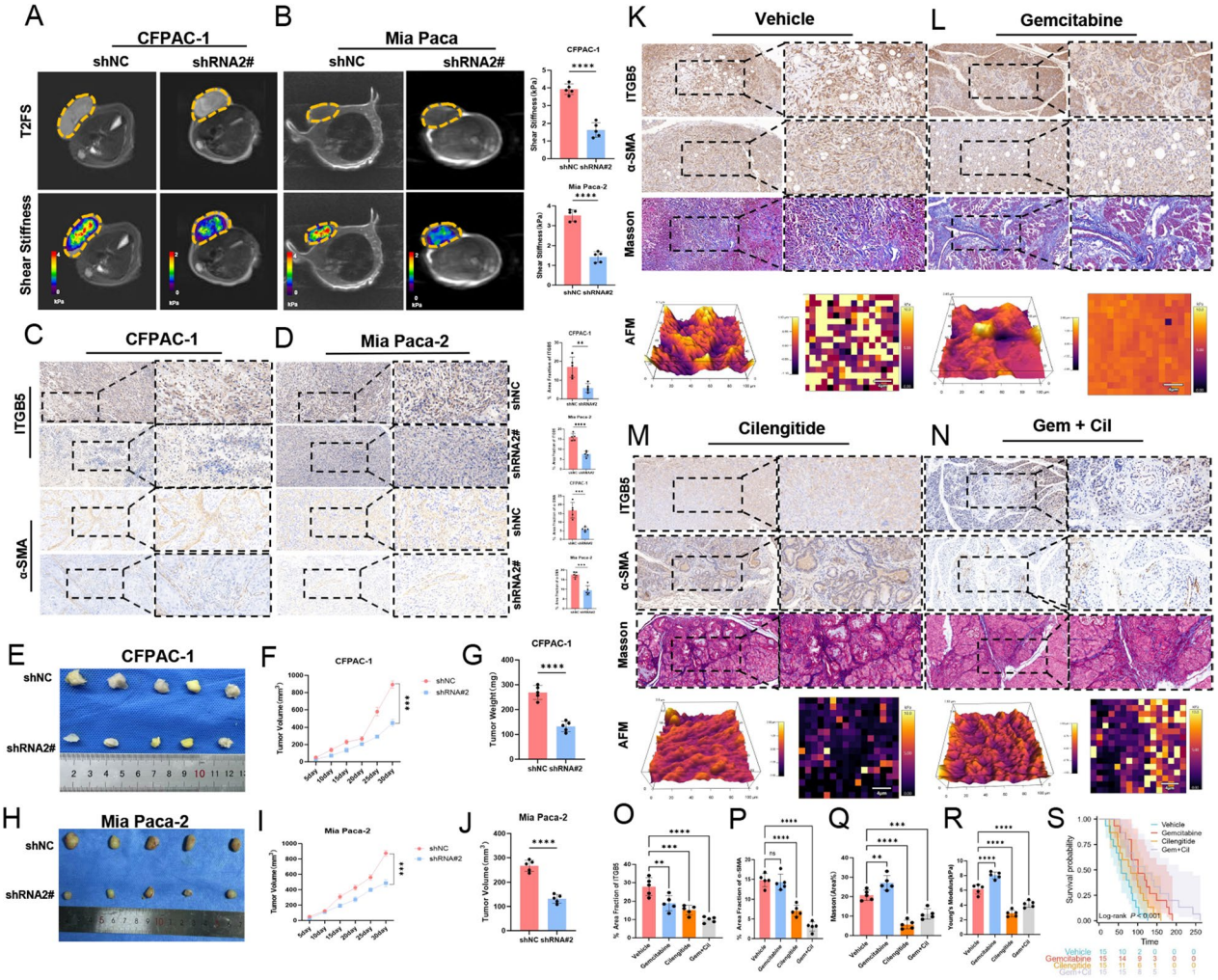


Fig. 7 ITGB5 promotes the malignant progression and biomechanics of PDAC in vivo. **A**–**B** MRE of subcutaneous xenograft tumors in nude mice. Top row: T2-FS anatomical images; bottom row: corresponding elastograms depicting tumor shear stiffness. **D** IHC for *ITGB5* and *α-SMA* expression in PDAC xenograft tumors. The first two rows show the staining results for *ITGB5*, with the first row at 200× magnification and the second row at 400× magnification. The last two rows show the staining results for *α-SMA*, with the third row at 200× magnification and the fourth row at 400× magnification. **E**–**G** CFPAC-1 xenograft results: **E** representative tumor images; **F** tumor growth curves (days vs. volume; growth-curve analysis: [model/test used]); **G** endpoint tumor volumes/weights. **H**–**I** MiaPaCa-2 xenograft results: **H** representative tumor images; **I** tumor growth curves; **J** endpoint tumor volumes/weights. **K**–**N**. Representative results of IHC, Masson's trichrome staining, and atomic force microscopy in the KPC model across the Vehicle, Gemcitabine, Cilengitide, and Gem + Cil groups. **O** Semiquantitative analysis of *ITGB5* expression levels in the Vehicle, Gemcitabine, Cilengitide, and Gem + Cil groups. **P** Semiquantitative analysis of *α-SMA* expression levels in the Vehicle, Gemcitabine, Cilengitide, and Gem + Cil groups. **Q** Semiquantitative analysis of Masson's trichrome staining in the Vehicle, Gemcitabine, Cilengitide, and Gem + Cil groups. **R** Statistical analysis of Young's modulus measured by atomic force microscopy on tissue sections from the Vehicle, Gemcitabine, Cilengitide, and Gem + Cil groups. **S** Perform survival analysis on mice in the Vehicle, Gemcitabine, Cilengitide, and Gem + Cil groups using the Log-rank test. For the analysis of continuous variables between two groups, the Mann–Whitney U test was used; for the analysis of continuous variables among more than two groups, the Kruskal–Wallis test was applied. Statistical significance between Kaplan–Meier curves was assessed using a two-sided log-rank test. A *p*-value < 0.05 was considered statistically significant

prior reports [24]). Despite increased collagen, *α-SMA* levels in Gemcitabine-treated tumors did not differ significantly from Vehicle (Fig. 7L, P, second row, $p > 0.05$). AFM measurements indicated that Gemcitabine-treated tumors had the highest tissue Young's modulus, whereas Cilengitide-treated tumors had the lowest; combination therapy attenuated Gemcitabine-induced stiffening (Fig. 7K–N, R, fourth row, all $p < 0.001$).

Alough Gemcitabine increased matrix stiffening, it improved survival; importantly, Gemcitabine + Cilengitide combination produced the greatest survival benefit (Fig. 7S, $p < 0.0001$). Collectively, these data indicate that targeting *ITGB5* reshapes PDAC tumor biomechanics in vivo, suppresses tumor progression, and may enhance therapeutic efficacy. Further studies are warranted to define the underlying mechanisms.

Discussion

PDAC is characterized by pronounced tissue stiffness, which largely arises from the complexity of its TME [25]. CAFs play a central role in shaping this microenvironment [26]. CAFs suppress immune cell function through secretion of cytokines and metabolic mediators, thereby promoting tumor growth, invasion, and metastasis [27]. They also remodel the extracellular matrix (ECM) to form physical barriers that impede drug delivery and immune-cell infiltration [28]. In addition, CAFs are major determinants of the adverse biomechanical properties of PDAC. Therefore, modulating CAF phenotypes or overcoming their barrier function to inhibit tumor progression and normalize PDAC biomechanics represents a promising therapeutic strategy.

However, broad stromal-targeting approaches in clinical and preclinical studies have largely failed, underscoring the need for more precise, cell-type–specific stromal targets. In this study, using single-cell transcriptomic and bioinformatic analyses, we identified *ITGB5* as a CAF-enriched candidate therapeutic target in PDAC. Through complementary in vitro and in vivo experiments, we show that *ITGB5* promotes PDAC malignancy and that elevated ITGB5 expression is associated with poorer patient prognosis. Biomechanical assays demonstrated the *ITGB5* silencing significantly decreased key stiffens parameters, including shear stiffness measured by 3D-MRE and Young's modulus measured by AFM. These results indicate that *ITGB5* is a critical regulator of the biomechanical properties of PDAC.

Cilengitide is a cyclic RGD peptide antagonist of *αvβ3/αvβ5* integrins. Previous studies have shown that it can suppress *ITGB5(αvβ5)* expression in various tumors [29–31] and can inhibit CAF proliferation and remodel the tumor immune microenvironment to enhance antitumor cytotoxicity [32]. In PDAC models, improved delivery and release efficiency of Cilengitide has been shown to improve intratumoral perfusion, increase drug penetration, and thereby enhance cytotoxic effects on pancreatic cancer cells [33].

Gemcitabine, a first-line chemotherapeutic agent for PDAC [34], can prolong patient survival but is associated with significant toxicities. Recent study reported that gemcitabine exacerbates stromal fibrosis in PDAC [24], consistent with our own findings; increased fibrosis can impair drug penetration and compromise therapeutic efficacy.

In the KPC mouse model, we evaluated whether combining cilengitide with gemcitabine could target ITGB5/αvβ5-dependent CAF activity, remodel PDAC biomechanics, mitigate gemcitabine-induced fibrosis, and improve therapeutic efficacy and survival. We found that cilengitide treatment reduced stromal fibrosis in vivo. Cilengitide monotherapy provided limited survival benefit relative to gemcitabine, whereas the combination of cilengitide plus gemcitabine both attenuated fibrosis and significantly extended survival in KPC mice These results suggest that targeting ITGB5/αvβ5 with agents such as cilengitide may represent a viable stromal-targeted approach to enhance chemotherapy efficacy in PDAC. Further preclinical and mechanistic studies are warranted to define optimal dosing, delivery strategies, and safety.

In this study, we adopted tumor shear stiffness measured by 3D-MRE as a primary indicator of PDAC biomechanical characteristics. Previous biomechanical assessments of PDAC have typically relied on EUS, Shore durometer, or AFM. By contrast, 3D-MRE is a non-invasive clinically translatable modality for biomechanical assessment that has been infrequently applied to PDAC. To our knowledge, this is the first study to explore the relationship between shear stiffness measured by 3D-MRE and PDAC biomechanical properties regulated by *ITGB5*. Our results demonstrate that 3D-MRE can accurately detect biomechanical differences in PDAC, suggesting its broader utility beyond established applicationsin liver [35] and brain diseases [36, 37] to include PDAC biomechanical evaluation.

This study inevitably faces several challenges and limitations. First, our clinical cohort included only resectable PDAC patients who underwent primary surgery, which may limit generalizability to advanced or unresectable disease because tumor biomechanics and CAF subpopulation dynamics can differ by stage. Second, the clinical cohort comprised only 80 PDAC patients from a single center. Future multicenter prospective studies with larger patient cohorts are needed, as are phase I/II clinical trials of *ITGB5* inhibitors to further elucidate links between ITGB5 signaling and ECM stiffness in PDAC.

Future research should stratify CAFs by subtype—e.g., inflammatory CAFs (infCAFs), developmental CAFs (dCAFs), and reactive CAFs (rCAFs)—to identify which fibroblast subsets are directly modulated by *ITGB5*. Moreover, in addition to CAF-derived collagen, other ECM components such as hyaluronic acid also contribute to PDAC biomechanics. Our study focused on *ITGB5* effects on collagen deposition and did not evaluate its role in hyaluronic acid synthesis or binding [38]. The PDAC microenvironment is highly heterogeneous, and immune cells and other stromal components also participate in regulating tumor stiffness [39]. Integrated application of emerging technologies—single-cell RNA sequencing [40] and spatial transcriptomics [41], as well as organoid systems [42], patient-derived xenografts (PDX) [43], and integrated multi-omics [43] approaches—can provide spatially resolved single-cell insight, enable mechanistic validation in vitro and in vivo, and facilitate identification of key cell subsets, intercellular signaling pathways, and

translational targets. Here, we examined only the effects of *ITGB5*-knockdown in CAFs on PDAC cells but did not explore how *ITGB5* influences interactions between CAFs and other cell types such as immune or endocrine cells; Futher experiments are required to delineate how *ITGB5* shapes intercellular communicationin the PDAC microenvironment.

Finally, our current MRE setup does not support in vivo biomechanical measurements in KPC mice. Future work will explore higher-field MRI systems (e.g.,7T) and develop corresponding high-frequency mechanical wave drivers (e.g., ~ 1000 Hz) to enable in vivo detection of small tumors in KPC models.

In summary, this study highlights a central role for *ITGB5* in the PDAC stroma and demonstrates, for the first time, that targeting *ITGB5* in CAFs can modulate the PDAC matrix. In the KPC model, inhibition mitigated gemcitabine-exacerbated stromal fibrosis, decreased matrix stiffness, and improved survival. Methodologically, we propose 3D-MRE as a noninvasive tool for diagnosis and treatment monitoring to better characterize tumor mechanics and guide individualized stromal-targeted strategies. Collectively, these findings support further preclinical and translational evaluation of ITGB5-directed stromal therapies in PDAC.

Abbreviations

AFM	Atomic force microscopy
CAFs	Cancer-associated fibroblasts
ECM	Extracellular matrix
GEO	Gene expression omnibus
HS	High-stiffness
IHC	Immunohistochemistry
IQR	Interquartile range
ITGB5	Integrin beta-5
KM	Kaplan–Meier
MRE	Magnetic resonance elastography
MRI	Magnetic resonance imaging
OS	Overall survival
PDAC	Pancreatic ductal adenocarcinoma
PFI	Progress free interval
ScRNA-seq	Single-cell RNA sequencing
shRNA	Small hairpin RNA
shITGB5	Small hairpin RNA targeting ITGB5
TCGA	The Cancer Genome Atlas
T2FS	T2-weighted imaging with fat suppression
uMAP	Uniform manifold approximation and projection
LS	Low-stiffness
α-SMA	Alpha-smooth muscle actin

Supplementary Information

The online version contains supplementary material available at https://doi.org/10.1186/s12967-025-07119-5.

Supplementary Material 1

Acknowledgements
Not applicable.

Author contributions
Conceptualization, Y.A., G.L., and S.Y.; methodology, Y.A., P.C., G.C., L.B., L,L and S.Y.; investigation, Y.A., P.C., G.C., L.B., Z.X., H,W., Z.Y., L.Y. N., W,X.,and Z.M.; writing—original draft, Y.A., P.C., G.C., L.B., and S.Y.; writing—review & editing, all authors; funding acquisition, S.Y.; resources, S.Y., and G.F; supervision, S.Y., and G.F.

Funding
This work was supported by the National Natural Science Foundation of China (No. 82471971); Liaoning Province Science and Technology Joint Plan (2023JH2/101700127, 2023JH2/101700195); the Leading Young Talent Program of Xingliao Yingcai in Liaoning Province (XLYC2203037); Liaoning Provincial Science and Technology Program (2025-BS-0581).

Data availability
Data access can be obtained through a reasonable request to Yu Shi (20,072,265@cmu.edu.cn). Access to the data will be restricted to non-commercial research which removes patient-sensitive information. All requests will be answered within 10 working days.

Declarations

Ethics approval and consent to participate
This is a prospective single-center clinical trial registered in the U.S. Clinical Trials Database (https://clinicaltrials.gov/) under registration number NCT06526442 on October 9th, 2020. It complied with the Health Insurance Portability and Accountability Act and was approved by the Institutional Review Board (IRB) of Shengjing Hospital of China Medical University (Human Research Ethics Committee approval 2022PS1006K), with written informed consent obtained from all participants. Patients were recruited between January 2022 and September 2024. For murine experiments, all protocols adhered to the guidelines of the Institutional Animal Care and Use Committee (IACUC) and were approved by the Medical Ethics Committee of our local hospital (approval number 2023PS1082K).

Consent for publication
All authors have read and approved the final manuscript and consent to publication.

Competing interests
The authors declare no competing interests.

Author details
[1]Department of Radiology, Shengjing Hospital, China Medical University, Shenyang, Liaoning, China
[2]Liaoning Provincial Key Laboratory of Medical Imaging, Shenyang, , Liaoning, China
[3]School of Intelligent Medicine, China Medical University, Shenyang, Liaoning Province, China
[4]Department of Nuclear Medicine, Shengjing Hospital, China Medical University, Shenyang, Liaoning, China
[5]Department of General Surgery, Shengjing Hospital, China Medical University, Shenyang, Liaoning, China

Received: 29 July 2025 / Accepted: 9 September 2025
Published online: 21 October 2025

References

1. Siegel RL, Giaquinto AN, Jemal A. Cancer statistics, 2024. CA Cancer J Clin. 2024;74:12–49. https://doi.org/10.3322/caac.21820.
2. Hessmann E, Buchholz SM, Demir IE, Singh SK, Gress TM, Ellenrieder V, et al. Microenvironmental determinants of pancreatic cancer. Physiol Rev. 2020;100:1707–51. https://doi.org/10.1152/physrev.00042.2019.
3. Caligiuri G, Tuveson DA. Activated fibroblasts in cancer: perspectives and challenges. Cancer Cell. 2023;41:434–49. https://doi.org/10.1016/j.ccell.2023.02.015.
4. Zhu Z, Achreja A, Meurs N, Animasahun O, Owen S, Mittal A, et al. Tumour-reprogrammed stromal BCAT1 fuels branched-chain ketoacid dependency in

stromal-rich PDAC tumours. Nat Metab. 2020;2:775–92. https://doi.org/10.1038/s42255-020-0226-5.
5. Qi R, Bai Y, Li K, Liu N, Xu Y, Dal E, et al. Cancer-associated fibroblasts suppress ferroptosis and induce gemcitabine resistance in pancreatic cancer cells by secreting exosome-derived ACSL4-targeting miRNAs. Drug Resist Updat. 2023;68:100960. https://doi.org/10.1016/j.drup.2023.100960.
6. Jenkins L, Jungwirth U, Avgustinova A, Iravani M, Mills A, Haider S, et al. Cancer-associated fibroblasts suppress CD8+ T-cell infiltration and confer resistance to immune-checkpoint blockade. Cancer Res. 2022;82:2904–17. https://doi.org/10.1158/0008-5472.CAN-21-4141.
7. Weniger M, Honselmann KC, Liss AS. The extracellular matrix and pancreatic cancer: a complex relationship. Cancers (Basel). 2018. https://doi.org/10.3390/cancers10090316.
8. Hu D, Li Z, Zheng B, Lin X, Pan Y, Gong P, et al. Cancer-associated fibroblasts in breast cancer: challenges and opportunities. Cancer Commun (Lond). 2022;42:401–34. https://doi.org/10.1002/cac2.12291.
9. Nia HT, Munn LL, Jain RK. Physical traits of cancer. Science. 2020. https://doi.org/10.1126/science.aaz0868.
10. Zheng J-H, Zhu Y-H, Yang J, Ji P-X, Zhao R-K, Duan Z-H, et al. A CLIC1 network coordinates matrix stiffness and the Warburg effect to promote tumor growth in pancreatic cancer. Cell Rep. 2024;43:114633. https://doi.org/10.1016/j.celrep.2024.114633.
11. Cox TR. The matrix in cancer. Nat Rev Cancer. 2021;21:217–38. https://doi.org/10.1038/s41568-020-00329-7.
12. Yousaf MN, Chaudhary FS, Ehsan A, Suarez AL, Muniraj T, Jamidar P, et al. Endoscopic ultrasound (EUS) and the management of pancreatic cancer. BMJ Open Gastroenterol. 2020. https://doi.org/10.1136/bmjgast-2020-000408.
13. Massey AE, Doxtater KA, Yallapu MM, Chauhan SC. Biophysical changes caused by altered MUC13 expression in pancreatic cancer cells. Micron. 2020;130:102822. https://doi.org/10.1016/j.micron.2019.102822.
14. Belyaev O, Herden H, Meier JJ, Muller CA, Seelig MH, Herzog T, et al. Assessment of pancreatic hardness-surgeon versus durometer. J Surg Res. 2010;158:53–60. https://doi.org/10.1016/j.jss.2008.08.022.
15. Ozturk A, Olson MC, Samir AE, Venkatesh SK. Liver fibrosis assessment: MR and US elastography. Abdom Radiol (NY). 2022;47:3037–50. https://doi.org/10.1007/s00261-021-03269-4.
16. Idilman IS, Li J, Yin M, Venkatesh SK. MR elastography of liver: current status and future perspectives. Abdom Radiol. 2020;45:3444–62. https://doi.org/10.1007/s00261-020-02656-7.
17. Lei T, Lin Y, Lai X, Zhang Y, Ma Y, Wang X, et al. *ITGB5* facilitates gastric cancer metastasis by promoting *TGFBR2* endosomal recycling. Cancer Lett. 2024;592:216953. https://doi.org/10.1016/j.canlet.2024.216953.
18. Chan X-Y, Chang K-P, Yang C-Y, Liu C-R, Hung C-M, Huang C-C, et al. Upregulation of ENAH by a PI3K/AKT/β-catenin cascade promotes oral cancer cell migration and growth via an ITGB5/Src axis. Cell Mol Biol Lett. 2024;29:136. https://doi.org/10.1186/s11658-024-00651-0.
19. Huang L, Lu Y, He R, Guo X, Zhou J, Fu Z, et al. N4-acetylcytidine modification of *ITGB5* mRNA mediated by *NAT10* promotes perineural invasion in pancreatic ductal adenocarcinoma. J Exp Clin Cancer Res. 2025;44:103. https://doi.org/10.1186/s13046-025-03362-2.
20. Wen X, Chen S, Chen X, Qiu H, Wang W, Zhang N, et al. Corrigendum: ITGB5 promotes innate radiation resistance in pancreatic adenocarcinoma by promoting DNA damage repair and the MEK/ERK signaling pathway. Front Oncol. 2024;14:1381151. https://doi.org/10.3389/fonc.2024.1381151.
21. Song Q, Shi Y, Gao F, Yin M, Yang R, Liu Y, et al. Feasibility and reproducibility of multifrequency magnetic resonance elastography in healthy and diseased pancreases. J Magn Reson Imaging. 2022;56:1769–80. https://doi.org/10.1002/jmri.28158.
22. Laklai H, Miroshnikova YA, Pickup MW, Collisson EA, Kim GE, Barrett AS, et al. Genotype tunes pancreatic ductal adenocarcinoma tissue tension to induce matricellular fibrosis and tumor progression. Nat Med. 2016;22:497–505. https://doi.org/10.1038/nm.4082.
23. An H, Shi Y, Guo Q, Liu Y. Test-retest reliability of 3D EPI MR elastography of the pancreas. Clin Radiol. 2016. https://doi.org/10.1016/j.crad.2016.03.014.
24. Chitty JL, Yam M, Perryman L, Parker AL, Skhinas JN, Setargew YFI, et al. A first-in-class pan-lysyl oxidase inhibitor impairs stromal remodeling and enhances gemcitabine response and survival in pancreatic cancer. Nat Cancer. 2023;4:1326–44. https://doi.org/10.1038/s43018-023-00614-y.
25. Ho WJ, Jaffee EM, Zheng L. The tumour microenvironment in pancreatic cancer: clinical challenges and opportunities. Nat Rev Clin Oncol. 2020;17:527–40. https://doi.org/10.1038/s41571-020-0363-5.
26. Yang D, Liu J, Qian H, Zhuang Q. Cancer-associated fibroblasts: from basic science to anticancer therapy. Exp Mol Med. 2023;55:1322–32. https://doi.org/10.1038/s12276-023-01013-0.
27. Saw PE, Chen J, Song E. Targeting CAFs to overcome anticancer therapeutic resistance. Trends Cancer. 2022;8:527–55. https://doi.org/10.1016/j.trecan.2022.03.001.
28. Kennel KB, Bozlar M, De Valk AF, Greten FR. Cancer-associated fibroblasts in inflammation and antitumor immunity. Clin Cancer Res. 2023;29:1009–16. https://doi.org/10.1158/1078-0432.CCR-22-1031.
29. Zhang L, Gülses A, Purcz N, Weimer J, Wiltfang J, Açil Y. A comparative assessment of the effects of integrin inhibitor cilengitide on primary culture of head and neck squamous cell carcinoma (HNSCC) and HNSCC cell lines. Clin Transl Oncol. 2019;21:1052–60. https://doi.org/10.1007/s12094-018-02025-3.
30. Haddad T, Qin R, Lupu R, Satele D, Eadens M, Goetz MP, et al. A phase I study of cilengitide and paclitaxel in patients with advanced solid tumors. Cancer Chemother Pharmacol. 2017;79:1221–7. https://doi.org/10.1007/s00280-017-3322-9.
31. Stupp R, Hegi ME, Neyns B, Goldbrunner R, Schlegel U, Clement PMJ, et al. Phase I/IIa study of cilengitide and temozolomide with concomitant radiotherapy followed by cilengitide and temozolomide maintenance therapy in patients with newly diagnosed glioblastoma. J Clin Oncol. 2010;28:2712–8. https://doi.org/10.1200/JCO.2009.26.6650.
32. Chen W, Jiang M, Zou X, Chen Z, Shen L, Hu J, et al. Fibroblast activation protein (FAP)+ cancer-associated fibroblasts induce macrophage M2-like polarization via the fibronectin 1-integrin α5β1 axis in breast cancer. Oncogene. 2025;44:2396–412. https://doi.org/10.1038/s41388-025-03359-3.
33. Wei Y, Song S, Duan N, Wang F, Wang Y, Yang Y, et al. MT1-MMP-activated liposomes to improve tumor blood perfusion and drug delivery for enhanced pancreatic cancer therapy. Adv Sci. 2020;7:1902746. https://doi.org/10.1002/advs.201902746.
34. Stoop TF, Javed AA, Oba A, Koerkamp BG, Seufferlein T, Wilmink JW, et al. Pancreatic cancer. Lancet. 2025;405:1182–202. https://doi.org/10.1016/S0140-6736(25)00261-2.
35. Shi Y, Qi Y-F, Lan G-Y, Wu Q, Ma B, Zhang X-Y, et al. Three-dimensional MR elastography depicts liver inflammation, fibrosis, and portal hypertension in chronic hepatitis B or C. Radiology. 2021;301:154–62. https://doi.org/10.1148/radiol.2021202804.
36. Shi Y, Huo Y, Pan C, Qi Y, Yin Z, Ehman RL, et al. Use of magnetic resonance elastography to gauge meningioma intratumoral consistency and histotype. Neuroimage Clin. 2022;36:103173. https://doi.org/10.1016/j.nicl.2022.103173.
37. Fels-Palesandro H, Heuer S, Boztepe B, Streibel Y, Ungermann J, Pan C, et al. Assessment of tumor cell invasion and radiotherapy response in experimental glioma by magnetic resonance elastography. J Magn Reson Imaging. 2025;61:1203–18. https://doi.org/10.1002/jmri.29567.
38. Byeon HJ, Choi SH, Choi JS, Kim I, Shin BS, Lee ES, et al. Four-arm PEG cross-linked hyaluronic acid hydrogels containing PEGylated apoptotic TRAIL protein for treating pancreatic cancer. Acta Biomater. 2014;10:142–50. https://doi.org/10.1016/j.actbio.2013.08.046.
39. Perez-Penco M, Lara de la Torre L, Lecoq I, Martinenaite E, Andersen MH. TGFβ-specific T cells induced by a TGFβ-derived immune modulatory vaccine both directly and indirectly modulate the phenotype of tumor-associated macrophages and fibroblasts. J Immunother Cancer. 2024. https://doi.org/10.1136/jitc-2023-008405.
40. Chen K, Wang Q, Liu X, Tian X, Dong A, Yang Y. Immune profiling and prognostic model of pancreatic cancer using quantitative pathology and single-cell RNA sequencing. J Transl Med. 2023;21:210. https://doi.org/10.1186/s12967-023-04051-4.
41. Zhu J, Zhang K, Chen Y, Ge X, Wu J, Xu P, et al. Progress of single-cell RNA sequencing combined with spatial transcriptomics in tumour microenvironment and treatment of pancreatic cancer. J Transl Med. 2024;22:563. https://doi.org/10.1186/s12967-024-05307-3.
42. Li K, He Y, Jin X, Jin K, Qian J. Reproducible extracellular matrices for tumor organoid culture: challenges and opportunities. J Transl Med. 2025;23:497. https://doi.org/10.1186/s12967-025-06349-x.

43. Guo P, Fang H, Shi H, Zhang J, Song G, Fan C, et al. Metabolic, transcriptomic, and proteomic adaptations in pancreatic ductal adenocarcinoma-patient derived xenograft models across serial passages. J Transl Med. 2025;23:732. https://doi.org/10.1186/s12967-025-06787-7.

Publisher's note

Springer Nature remains neutral with regard to jurisdictional claims in published maps and institutional affiliations.